IECO International Journal Of Industrial Electronics Control and Optimization
Print ISSN: 3517-2645
Online ISSN: 3568-2645
Homepage: https://ieco.usb.ac.ir/

A Multiport Isolated Resonant LLC Converter for Grid-Tied Renewable Energy Powered Bidirectional EV Charger

Nasim Bagheri[1]| Hasan Alipour[2]|Leila Mohammadian[3]|Jamal Beiza[4]| Mohsen Ebadpour[5]

Department of Electrical Engineering, Shabestar Branch, Islamic Azad University, Shabestar, Iran.[1,2,3,4,]
Department of Electrical Engineering, Ahar Branch, Islamic Azad University, Ahar, Iran[5].
Corresponding author's email: Hasan.alipour2006@gmail.com

Article Info

Article type:
Research Article

Article history:
Received: 2022-Sep-26
Received in revised form: 2023-Jan-03
Accepted: 2023-Feb-12
Published online: 2023-Feb-12

Keywords:
DC-DC converter,
Multiport,
Photovoltaic (PV) system,
Plug-in electric vehicles (PEVs),
Battery,

ABSTRACT

This paper proposes an integrated bidirectional multiport DC-DC converter for battery charging of plug-in electric vehicles, which can integrate the photovoltaic (PV) system, traction batteries, and the AC grid. The presented converter is more reliable than the conventional topologies because both PV panels and the grid can simultaneously or separately deliver power to high-voltage batteries. In addition, the topology is bidirectional and can transfer power from batteries to the AC grid by employing a half-bridge CLLC converter with fewer switches. Moreover, a unified controller along with optimum maximum power point tracking (MPPT) algorithm is utilized to control the converter. The converter topology, control system, and operating scenarios are analyzed by using state space modeling. The performance of the whole system is evaluated by testing the converter's operation in different conditions using MATLAB/Simulink software. The simulation results demonstrate that the proposed converter can not only control the charge and discharge of the batteries according to the state of the charge, but it can also maintain the DC-link voltage of the grid side to be in constant level.

I. Introduction

Nowadays, two widespread future trends in energy consumption are the rise in distributed renewable resources such as solar energy and the emergence of electric vehicles (EVs) as a green mode of transportation. Meanwhile, the integration of these two technologies faces more challenges in practice [1]. Firstly, EVs are zero-emission as long as the source of power is green. In addition, photovoltaic (PV) energy resources suffer from seasonal changes, so they entail a need for energy storage systems [2]. Furthermore, some voltage issues like overloading can occur in the power grid due to the overuse of distributed power resources and raised power demand of vehicle batteries [3-5]. To solve these problems, charging EVs with solar energy can be a decent solution that leads to net-zero emissions.

Integrating power sources has acquired universality in transportation electrifications. For this integration, the focus has been put on power electronic interfaces to enable the proper usage of energy systems. Plug-in electric vehicles (PEVs) vastly include three-phase battery chargers for their propulsion systems [6]. A typical traction battery charger topology contains an AC-DC power factor correction (PFC) converter, an isolated (transformer-equipped) or non-isolated DC-DC converter, and a power grid or a PV system as its input [7]. Several integrated DC-DC converter topologies have been presented for PEV battery chargers which can also interface renewable energy resources like solar system and the grid. A large number of the integrated converters are presented for single-phase system in which the power level is restricted by the range of the output voltage and current [8].

Different researchers have proposed non-isolated converters [9] that utilize a single switch [10]. In [11],

researchers use a hybrid of buck and boost converters to hybridize PV and battery systems. A soft-switched non-isolated three-port DC-DC topology is presented for a high-voltage gain converter using coupled inductors in [12]. Several previously established topologies are based on half-bridge converters for various applications such as transportation [13]. Other cases have established the hybridization of onboard multiport DC-DC converters for integrated energy systems. In [14], a pulse width modulation (PWM) strategy with a phase shift control method is used to integrate multiport converters. An onboard battery charger for EVs with the possibility of auxiliary feeding mode is presented in [15]. However, these topologies require complex electric circuits with more switching devices that cannot arrange isolations among the power network DC-link, traction batteries, and other energy sources as inputs of the converter [16]. The sliding mode control of LLC resonant DC-DC converter for a vast range of output voltage is presented for battery charging applications in [17]. The proposed controller operates at two switching frequencies for charging the EV batteries. The sliding mode control is a robust strategy for converter output voltage regulation with minimum distortion under a wide variation of input voltage, but it suffers from the chattering phenomenon, which deteriorates the overall system efficiency.

On the other hand, various topologies have been established using isolated DC-DC converters [18-20]. Some authors have focused on controlling the switching devices of the converter by employing different modulation methods such as pulse-frequency modulation [21] or phase-shift modulation with PWM [22]. There are other converter structures, such as half-bridge topologies [23] or coupled inductors controlled by phase-shift modulation [24]. Furthermore, bidirectional multiport resonant DC-DC converters are presented for vehicle-to-grid (V2G) operation and grid-to-vehicle (G2V) mode in PEV applications. However, some of them are unable to raise voltage gain and include circulating current between traction batteries and the power grid which deteriorates the grid current and induces unaccepted harmonic distortions [25]. In this regard, a new bidirectional multiport converter is presented in [26] which can be utilized as a converter that is installed in parking lots of intelligent places to provide power for local DC loads, such as DC home appliances and charge-connected EVs, simultaneously. The presented converter can act in G2H/G2VH/V2H/V2G scenarios. The topology is, however, very complicated and lowly reliable.

Other researchers have studied isolated CLLC topologies for battery chargers that contain discrete inductors, which escalate the size and cost of the converter circuit [27-29].

This paper presents an isolated multiport DC-DC converter for bidirectional EV battery chargers that can operate in PV-to-vehicle (PV2V), PV-to-grid (PV2G), G2V, and V2G modes. The modeling and analysis of the integrated converter for charging PEVs and also the hybridization of the PV system with traction batteries and the grid are the main considerations in this study. To reduce the volume and overall cost of the topology, the proposed resonant converter utilizes leakage inductance at the secondary and tertiary sides of the isolating transformer with no need for additional elements. Based on the presented model, several operation scenarios and modes are analyzed to better understand the converter's performance. PV panels can be mounted on the roof of parking areas as a stand-alone electric parking lot using the proposed converter to charge the vehicle with maximum solar power. The overall properties of the proposed topology and the contributions of this paper can be summarized as follows:

1) Isolation is provided among the PV array, the grid, and vehicle batteries.

2) A multi-output strategy is used for charging the traction batteries to rise the converter's reliability and efficiency.

3) There is no need for discrete inductors resulting in reduced size and cost of the converter circuit.

4) Using a comprehensive MIMO controller along with a proper maximum power point tracking (MPPT) control method to expand the voltage range.

5) A bidirectional battery charger that is capable of PV2G and V2G operation is designed and developed.

This manuscript is organized into six sections. Section II introduces the whole structure and operation modes of the converter. Operation principles and mathematical equations are expressed in detail in Section III. Section IV deals with the proposed control system. The complete simulation results considering the proposed control topology are given in Section V. Section VI summarizes the system performance, verifies the results, and provides some conclusions.

II. The Proposed Topology and Operation Scenarios

Conventional PEVs include a DC-AC inverter to feed the traction motor drive while the battery charger contains an AC-DC rectifier. The proposed converter improves them as an integrated bidirectional AC-DC and DC-DC converter, which can deliver power to the vehicle battery from a DC energy source, such as PV panels and the grid. The overall topology of the proposed converter is displayed in Fig. 1. As depicted in Fig. 1, a CLLC converter interfaces the battery port and the grid with a minimum number of switching devices, which can convey current using its symmetrical structure and the leakage inductance of three-winding integrated transformer [30]. Furthermore, the presented topology operates more stable than similar proposed multiport converters [30] since in the absence of the grid, PV arrays can charge the battery without any interruption (PV2V scenario). Hence, the AC grid can deliver power to the vehicle (G2V scenario) and also receive power from both PV panels (PV2V scenario) as an axillary power source and traction battery (V2G scenario) as an energy storage. Based on the proposed converter topology, the

isolated converter splits the DC-link capacitors into two center points connected to the transformer for reducing the stress of current and decreasing the differential mode conduction losses.

One of the attractive characteristics of the multiport boost converter is its simplicity. In essence, the proposed topology operates as a conventional boost converter that can swap its inputs and outputs. In comparison with conventional isolated converters, such as phase-shifted and LLC converters, the presented converter includes most advantages of the LLC converter such as soft switching at small loads and no need for an inductor of the output filter. Furthermore, the presented isolated topology enables intertwining an LLC resonant structure with the CLLLC converter by employing the tertiary winding of the isolated transformer when the vehicle charger operates in V2G modes. According to Fig. 1, the primary winding of the transformer is connected to the PV port while the secondary winding is coupled to the battery port. The third winding is connected to the AC grid. To properly obtain the converter parameters, it is necessary to correctly choose the turns ratio of the integrated transformer [30]. The core size of the transformer in practical applications is determined according to the switching frequency, voltage, and current level. This integrated converter rises the usage of the transformer, capacitors, and switching devices. Employing an electromagnetic integrated transformer with high inductance can (1) eliminate the external inductors, (2) decrease the converter volume, and (iii) reduce magnetic component losses. Modifications of the magnetic-core shapes and winding topologies have been studied in recent years, but this study is the first movement toward the integration of two leakage inductances in a three-winding transformer.

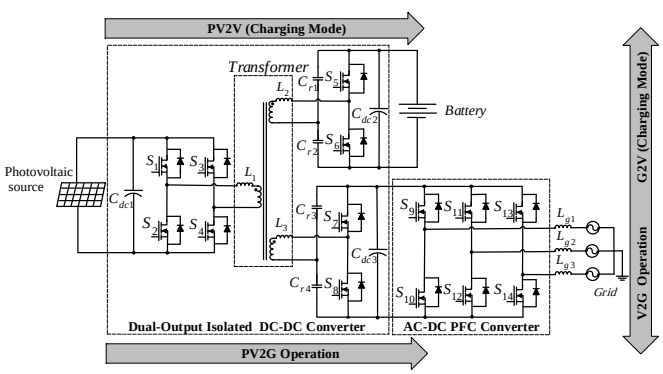

Fig. 1. The topology of the proposed multiport DC-DC converter

As Fig. 1 shows, the isolated structure includes two half-bridge converters at the secondary and tertiary sides of the transformer to lower the number of switching devices. Instead, the PV port at the primary side is equipped with a full-bridge converter to reduce the circulating current. Based on the proposed topology, the AC grid can deliver current to the batteries and also connect to PV arrays to acquire power. Moreover, the bidirectional PFC converter with switches ($S_9 \sim S_{14}$) is employed to improve the system's overall power quality and interface the AC grid.

Fig. 2. shows several operation scenarios of the converter. To reduce the voltage and current stresses of capacitors to around half, the resonant capacitors ($C_{r1} \sim C_{r4}$) deliver half resonant current in all scenarios. According to Fig. 2, for the bidirectional operation of the converter, the inductances (L_2 and L_3) of the isolating transformer act as the resonant inductors. Hence, C_{r1}, C_{r2}, and L_2 elements consist of a resonant circuit in scenarios I and IV whereas C_{r3}, C_{r4}, and L_3 elements lead to a resonant converter in scenarios II and III. Simultaneously conducting switches of the three ports is to be avoided in the proposed converter.

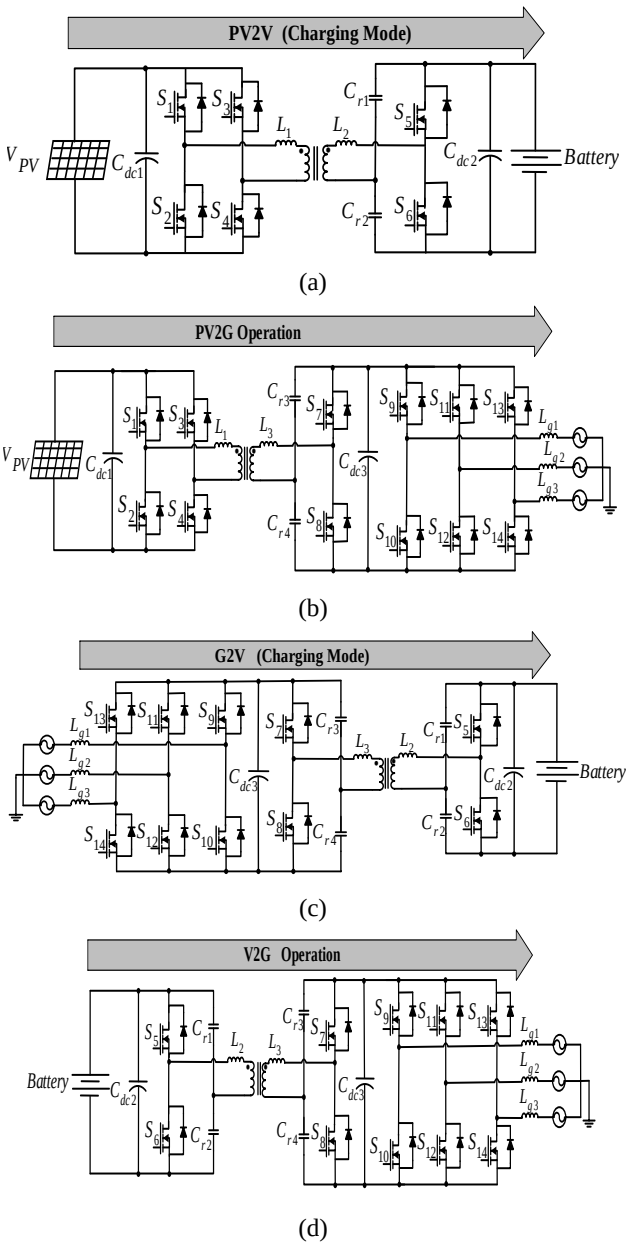

Fig. 2. The operation states for the isolated multiport converter: (a) Scenario I (PV2V), (b) Scenario II (PV2G), (c) Scenario III (G2V), (d) Scenario IV (V2G).

III. Operation Modes and Variables

To model and analyze the proposed converter's performance, the main variables and operation modes are

studied in detail. Since the voltage and current of the PV side are regulated by an MPPT controller, the system state variables can be expressed as

$$X^T = [i_{L1} \quad V_{Cdc3} \quad i_{L3} \quad i_{L2}]^T = [x_1 \quad x_2 \quad x_3 \quad x_4]^T \tag{1}$$

where $i_{L1\sim3}$ are the currents of the transformer inductances and v_{Cdc3} is the DC-link capacitor voltage of the AC grid.

To extract the averaged state-space model of the system, the state vectors during each scenario should be chosen. The detailed model of each scenario is described below.

A. Scenario I: PV to Vehicle (PV2V)

In Fig. 3, the current paths of the PV2V scenario are illustrated for different operation modes of the converter. As can be seen in Fig. 3(a), in scenario I in mode 1, switches S_1, S_4, and S_5 are delivering current to the battery from PV voltage (V_{PV}) through inductors L_1 and L_2 and capacitors C_1 and C_2. One of the system state variables (i_{L1}) which derivates from the PV current (I_{PV}) during mode 1 can be calculated with (2) by applying Kirchhoff's voltage low (KVL) through the red-arrowed current path (Fig. 3(a)) on the battery side.

$$v_{T2} = V_B - v_{L2} - v_{C2} \tag{2}$$

Applying Kirchhoff's voltage low for the red-arrowed current path on the PV side based on Fig. 3(a) can result in Eq. (3).

$$-V_{PV} + L_1 \dot{i_{L1}} + \frac{n_1 v_{T2}}{n_2} = 0 \tag{3}$$

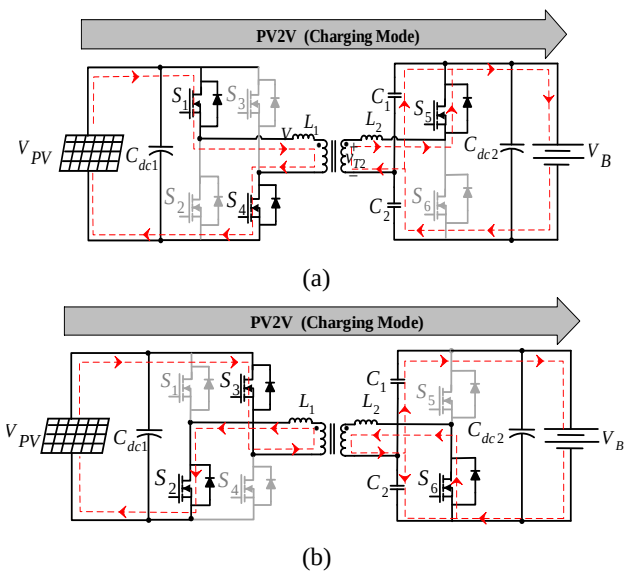

Fig. 3. The operation principles over PV2V scenario I: (a) Mode 1, (b) Mode 2

By combining Eq. (2) and (3), the averaged state-space equation in this mode can be found as follows

$$\dot{i_{L1}} = \frac{1}{L_1} V_{PV} - \frac{n_1}{n_2 \; L_1}(V_B - v_{L2} - v_{C1}) \tag{4}$$

where v_{T2} denotes the inducted voltage referred to the battery sides of the transformer, n_1/n_2 is its turn ratio, V_B is the battery voltage, v_L denotes the voltage across the leakage inductances of the transformer, and v_{C1} is the voltage of capacitor C_1.

Since the proposed converter plays the role of a charger in this scenario, the battery voltage is equal to

$$V_B = \frac{n_2}{n_1}(V_{PV} - v_{L1}) + v_{L2} + v_{C2} \tag{5}$$

According to Fig. 3(b), switches S_2, S_3, and S_6 deliver power to the battery by V_{PV} using inductors L_1 and L_2 and capacitors C_1 and C_2 during the second mode in scenario I. i_{L1} during mode 2 can be determined as

$$V_B + v_{L2} + v_{T2} - v_{C1} = 0 \tag{6}$$

$$-V_{PV} - L_1 \dot{i_{L1}} - \frac{n_1 v_{T2}}{n_2} = 0 \tag{7}$$

$$\dot{i_{L1}} = -\frac{1}{L_1} V_{PV} - \frac{n_1}{n_2 \; L_1}(v_{C1} - V_B - v_{L2}) \tag{8}$$

The battery voltage can be calculated as

$$V_B = \frac{n_2}{n_1}(V_{PV} + v_{L1}) - v_{L2} + v_{C1} \tag{9}$$

B. Scenario II: PV to Grid (PV2G)

Regarding to Fig. 4, during mode 3 of scenario II (Fig. 4(a)), switches S_1, S_4, and S_7 of the converter and S_9, S_{12}, and S_{14} of the PFC inverter deliver current from the PV port to the AC grid via inductors L_1 and L_3 and capacitor C_4. V_{Cdc3} (grid side DC-link voltage) as the second state variable of the converter in mode 3 can be written as

$$v_{T3} = -v_{L3} + v_{Cdc3} - v_{C4} \tag{10}$$

$$-V_{PV} + \frac{n_1 v_{T3}}{n_3} + L_1 \dot{i_{L1}} = 0 \tag{11}$$

$$v_{Cdc3} = v_{L3} + v_{C4} + \frac{n_3}{n_1}(V_{PV} - L_1 \dot{i_{L1}}) \tag{12}$$

As shown in Fig. 4(b), switches S_2, S_3, and S_7 of the converter and S_9, S_{12}, and S_{13} on the inverter port convey PV current to the AC grid using inductors L_1 and L_3 and capacitor C_3 in mode 4. The variable V_{Cdc3} during mode 4 can be expressed as

$$v_{T3} = -v_{L3} - v_{Cdc3} + v_{C3} \tag{13}$$

$$-V_{PV} - \frac{n_1 v_{T3}}{n_3} - L_1 \dot{i_{L1}} = 0 \tag{14}$$

$$v_{Cdc3} = -v_{L3} + v_{C4} + \frac{n_3}{n_1}(V_{PV} + L_1 \dot{i_{L1}}) \tag{15}$$

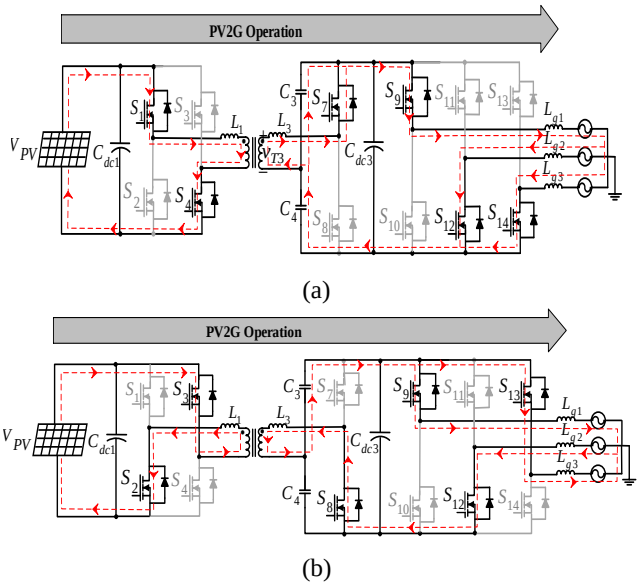

(a)

(b)

Fig. 4. The operation principles of PV2G modes: (a) Mode 3, (b) Mode 4

C. Scenario III: Grid to Vehicle (G2V)

Based on Fig. 5(a), switches S_5 and S_7 and also inverter switches S_{10}, S_{11}, and S_{14} conduct current to charge the vehicle from the AC grid by inductors L_2 and L_3 and capacitors C_1 and C_4 in mode 5. Another state variable of the converter (i_{L3}) which derivate from the AC grid current (I_G) in mode 5 can be determined as

$$v_{C4} + v_{T3} + L_3 \dot{i_{L3}} - v_{Cdc3} = 0 \tag{16}$$

$$v_{T2} = V_B - v_{C2} - v_{L2} \tag{17}$$

$$\dot{i_{L3}} = \frac{1}{L_3}(v_{Cdc3} - v_{C4}) - \frac{n_3}{n_2\ L_3}(\mathrm{V}_B - v_{C2} - v_{L2}) \tag{18}$$

In this scenario, the traction battery is also charged from the grid and the battery voltage can be found as

$$\mathrm{V}_B = \frac{n_2}{n_3}(v_{Cdc3} - v_{C4} - v_{L3}) + v_{C2} + v_{L2} \tag{19}$$

Similarly, over mode 6 (see Fig. 5(b)), differential equations can be expressed as

$$v_{T2} = -V_B + v_{C1} - v_{L2} \tag{20}$$

$$\dot{i_{L3}} = \frac{1}{L_3}(v_{Cdc3} - v_{C4}) - \frac{n_3}{n_2\ L_3}(\mathrm{V}_B - v_{C1} + v_{L2}) \tag{21}$$

$$\mathrm{V}_B = \frac{n_2}{n_3}(v_{Cdc3} - v_{C4} - v_{L3}) + v_{C1} - v_{L2} \tag{22}$$

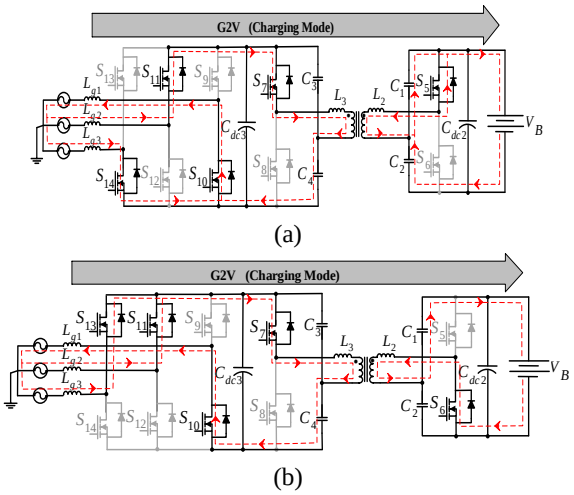

(a)

(b)

Fig. 5. Operation principles during G2V modes: (a) Mode 5, (b) Mode 6

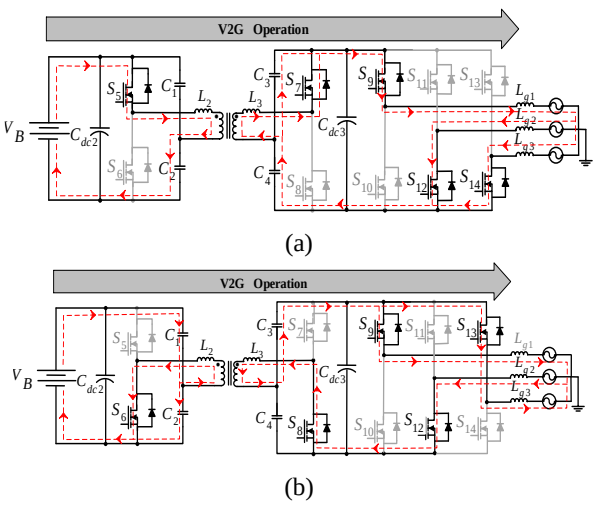

(a)

(b)

Fig. 6. The converter's performance over V2G scenario: (a) Mode 7, (b) Mode 8

D. Scenario IV: Vehicle to Grid (V2G)

According to Fig. 6(a), converter switches S_5 and S_7 and inverter-side switches S_9, S_{12}, and S_{14} are switched ON to deliver current from the vehicle to the grid by inductors L_2 and L_3 and capacitors C_2 and C_4. Then, the other variable of the converter (i_{L2}) which derivates from the battery current (I_B) during mode 6 is obtained as

$$\dot{i_{L2}} = \frac{1}{L_2}(\mathrm{V}_B - v_{C2}) - \frac{n_2}{n_3\ L_2}((v_{Cdc3} + v_{L3} + v_{C3}) \tag{23}$$

Similarly, based on Fig. 6(b), in mode 8, i_{L2} can be calculated as

$$\dot{i_{L2}} = \frac{1}{L_2}(v_{C2} - \mathrm{V}_B) + \frac{n_2}{n_3\ L_2}((v_{Cdc3} + v_{L3} - v_{C3}) \tag{24}$$

Owning to the explained operation modes, the isolated multiport converter can transfer power from and to different ports. To conclude the operation modes, Table 1 lists the switching patterns of the converter for each operation mode.

TABLE 1
THE OPERATION MODES AND PATTERNS OF CONVERTER SWITCHING FOR DIFFERENT SCENARIOS

Scenario	Mode	DC-DC Converter switches states								Charging mode
		S_1	S_2	S_3	S_4	S_5	S_6	S_7	S_8	
I	1	1	0	0	1	1	0	0	0	Yes
	2	0	1	1	0	0	1	0	0	
II	3	1	0	0	1	0	0	1	0	No
	4	0	1	1	0	0	0	0	1	
III	5	0	0	0	0	1	0	1	0	Yes
	6	0	0	0	0	0	1	1	0	
IV	7	0	0	0	0	1	0	1	0	No
	8	0	0	0	0	0	1	0	1	

IV. The Control of the Proposed Converter

The applied control strategy ensures that the current delivered to/from the grid is near sinusoidal with accepted quality and in phase. The overall block diagram of the studied converter's control strategy is shown in Fig. 7 in which to regulate the battery voltage, the voltages of the DC links must be fixed and the gain of the converter is appropriately adjusted. There is a unified multifunctional controller for PFC and DC-DC converters which is described in detail in this section. Since the converter operation depends on the aforementioned state variables, according to Fig. 7, the first state variable i_{L1} is controlled by the MPPT block through I_{PV}, v_{Cdc3} is regulated by the voltage PI controller, i_{L3} is controlled by the PFC inverter controller, and the last state variable i_{L2} is controlled by the battery-side current PI controller through I_B. Voltage and current controllers are employed to provide effective performance in adjusting DC values and then zero steady-state errors.

A. MPPT Controller for PV port

Since the PV cell suffers from environmental conditions such as irradiance level and surrounding temperature, to improve the efficiency of the PV system, the MPPT controller is necessary. For MPPT, the duty cycle of PV-side converter switches can be found by an appropriate definition of the error signal that comes from a closed-loop controller. Common MPPT approaches like constant voltage tracking (CVT) [31], incremental conductance (INC) scheme [32], and the Perturb and Observe (P&O) method [30] are presented. The CVT method has low accuracy and reliability due to voltage stabilizing rather than MPPT. Both the INC and the P&O methods can fluctuate near the maximum power point, normally an adaptive step to acquire better performance.

The proposed converter employs the INC algorithm-based MPPT control which is implemented using an integral controller to maximize the PV panel's output power. The basic concept of the INC approach is that the slope of the Power-Voltage (P-V) characteristics of the PV module which is illustrated in Fig. 8 is zero at maximum power points. It can be obtained from Fig. 8 that the condition for achieving maximum power at the peak point of the curve can be derived from the PV system output power as follows

$$\frac{dP_{PV}}{dV_{PV}} = \frac{d(V_{PV} I_{PV})}{dV_{PV}} = I_{PV} + V_{PV} \frac{dI_{PV}}{dV_{PV}} = 0 \tag{25}$$

The maximum power point is obtained by satisfying

$$\frac{dI_{PV}}{dV_{PV}} = -\frac{I_{PV}}{V_{PV}} \tag{26}$$

In numerical studies, the differential of PV voltage and current (V_{PV} and I_{PV}) can be calculated as

$$\begin{cases} dI_{PV} = I_{PV}(k) - I_{PV}(k-1) \\ dV_{PV} = V_{PV}(k) - V_{PV}(k-1) \end{cases} \tag{27}$$

where *k* is the time interval. The essence of defining the maximum power points by the INC method is to determine the optimum working point that satisfies Eq. (26).
There are three criteria in the process of the INC algorithm as follows

$$\begin{cases} 1) \text{ if } dI_{PV} / dV_{PV} > -I_{PV} / V_{PV} \text{ then increase } V_{PV} \\ 2) \text{ if } dI_{PV} / dV_{PV} < -I_{PV} / V_{PV} \text{ then decrease } V_{PV} \\ 3) \text{ if } dI_{PV} / dV_{PV} = -I_{PV} / V_{PV} \text{ then unchange } V_{PV} \end{cases} \tag{28}$$

To achieve the criteria in Eq. (28), a PI controller is employed to minimize the MPPT error. According to Fig. 9, the MPPT block takes the PV cell voltage and current as its inputs and regulates them to properly switch the PV-side converter gates. Then, when the solar irradiance varies, the MPPT controller adjusts the output based on the new maximum power point.

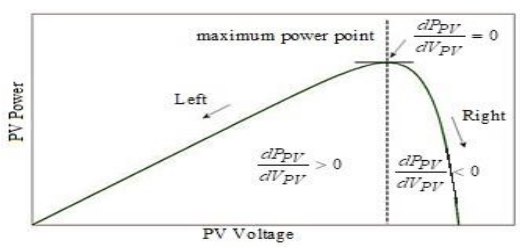

Fig. 8. The P-U characteristics of the PV module based on the INC concept

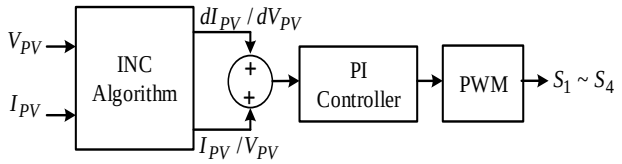

Fig. 9. The block diagram of the MPPT controller

B. PFC Inverter Controller

The control diagram of the PFC boost rectifier is depicted in Fig. 10. The PFC controller can secure the sinusoidal input from the AC grid current which results in a unity power factor and regulates the output voltage ($v_{C_{dc3}}$) at a constant desired level ($V_{dc,ref}$). The control scheme contains an inner current loop for the grid synchronization, an outer voltage loop for controlling $v_{C_{dc3}}$, and a three-phase phase-locked loop (PLL) to extract the grid voltage phase angle ($\phi = \omega t$). The extracted phase angle is applied to dq0 to abc Park's transformation and for synchronizing injected currents with grid voltages using the error signal of the AC-side DC-link controller (I_{d_ref}) . The control method is implemented using the dq0 synchronous reference frame which converts the grid quantities to DC values (v_{dq_mes} and i_{dq_mes}) to make the control easier.

The required active power is set by the direct axis reference current I_{d_ref} while the needed reactive power is determined using the quadrature axis reference current I_{q_ref} which is set to zero to make the unity power factor. The output voltages of the current regulator block are converted back to the abc values to serve as the reference signals utilized by the PWM pulse generator.

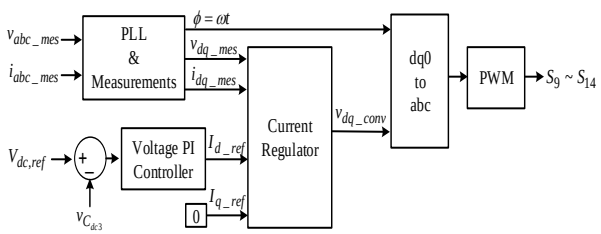

Fig. 10. The PFC controller's block diagram

C. Scenario Selection Scheme

The most important part of the control strategy is the scenario selection part, which allows the battery to be charged first from the solar cells and also allows it to be charged or discharged from/to the grid, as shown in Fig. 11. According to Table I, the control method mainly chooses scenario I (stand-alone operation) and scenario III (grid-connected operation) or both (PV2V + G2V), which makes the battery to be charged. Since the vehicle is never driven during plugged-in, the two charging scenarios can be separated by the scenario selection algorithm. This makes the converter operate in several modes with different scenarios. Furthermore, in contrast to the last established multiport converters which widely depend on the grid [30], the proposed control method enables the converter to perform as an off-grid and/or a grid-connected charger which can elevate charger reliability.

To extend the performance of the charger ports over the entire range of voltage, two variable DC-links ($v_{C_{dc2}}$ and $v_{C_{dc3}}$) are capable of delivering power to the vehicle. Considering Fig. 7, to minimize the errors in the control strategy between the reference values and measured amounts, standard PI controllers are employed.

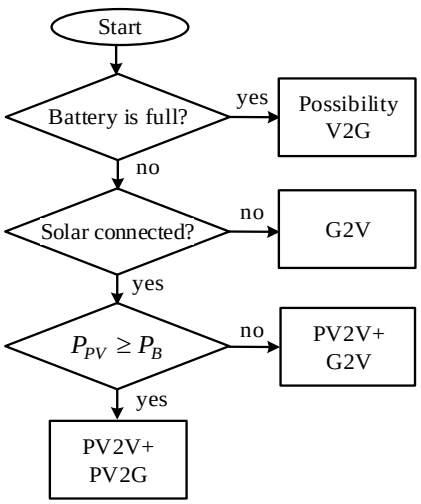

Fig. 11. The PFC scenario selection flowchart diagram

V. Simulation Results and Discussions

To test the proposed converter's operation and control methodology, the whole topology is built and simulated in MATLAB/Simulink environment. The major parameters of the converter elements are shown in Table 2. SunPower SPR-415E-WHT-D PV arrays are used for PV systems whose module parameters under specification standard test conditions (temperature = 25ºC, irradiation = 1000 W/m^2) are shown in Table 3. The voltage of the vehicle battery can be varied from 240 to 420 V, and the DC-link voltage of the grid side is controlled from 300 V to 600 V. The switching frequency of devices changes from 180 kHz to 200 kHz. The gain of the PI controllers is obtained through a trial-and-error procedure.

TABLE 2
MAIN PARAMETERS OF THE CONVERTER USED IN THE SIMULATION

Component	value
L_1	64 uH
L_2	38 uH
L_3	85 uH
N1:N2:N3	40:20:30
C_{r1} , C_{r2}	10 uF
C_{r3} , C_{r4}	5 uF

TABLE 3
PV MODULE PARAMETERS

parameter	**value**
Open-circuit voltage	64.2 V
Short-circuit current	5.96 A
Maximum power point voltage	54.7 V
Maximum power point current	5.58 A
Maximum power	305.27 W
Number of series-connected modules per string	5
Number of parallel strings	66
Number of cells per module	96

To test the steady state and dynamic performance of the PV arrays under different conditions of disturbance in solar irradiation at standard temperature, two types of irradiation changes, first ramp changes and then severe step disturbances are studied. In the first study, the solar radiation is slowly changed and the PV cells are subjected to ramp variations as shown in Fig. 12 to evaluate the profile of output power and voltage which come from PV arrays. According to Fig. 12, initial solar radiation is set to 1000 W/m^2 and can generate power of about 24 kW. Based on Fig. 12(b), the DC-link voltage of the PV side quickly reaches its reference value of 480 V due to proper tuning of the MPPT controller. To assess the dynamic response of the system, at time 0.4 s, the irradiance changed slowly and dropped to 200 W/m^2 which makes power track this change and settle down around 0.15 s. Regarding the scenario selection algorithm, during time 0.8 s to 1 s, the PV power is decreased and the converter operates in scenario III to charge the vehicle battery from the AC grid through the PFC inverter. To operate in scenario, I, the solar irradiance rose to 600 W/m^2 at t=1 s, leading to an increase in power to around 14.5 kW. Considering Fig. 12, it can be seen that after all disturbances in solar irradiation, both PV power and voltage settle down in their reference values by employing the ideal maximum power tracking algorithm.

To examine the performance of the PV system under extreme changes in solar irradiation, the array is subjected to sudden step variations as depicted in Fig. 13. Similar to the first test, at t = 0.4 s, the irradiation suddenly dropped to 400 W/m^2 then increased to 800 W/m^2. The DC link voltage reaches the desired steady state values during all these severe variations as illustrated in Fig. 13 (b). Based on Fig. 13(c), the PV output power followed the changes and settled with about a 60-ms delay. Since temperature changes in modules can also affect the PV outputs, the system reactions to the temperature step variations are also tested here. Fig. 14 shows the PV port responses to the temperature changes at constant standard irradiation of 1000 W/m^2. According to Fig. 14(a), the initial PV array temperature is 25^{o}C which leads to the generation of 24 kW power based on Fig. 14(c). At t = 0.4 s, the temperature increased to 40^{o}C and the PV power tracked this change by a little reduction in voltage and power. At t=1 s, the temperature dropped to 15^{o}C, boosting the voltage and power. Hence an increase in temperature can slightly reduce the PV output voltage and power.

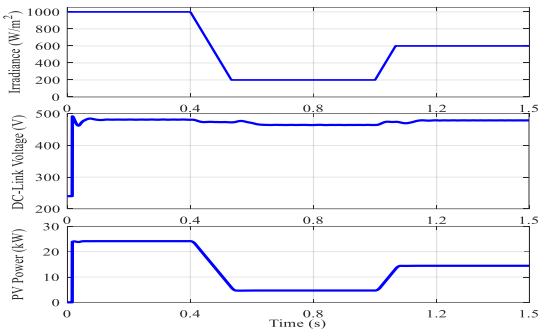

Fig. 12. The PV system's responses to ramp variations. (a) Solar radiation, (b) PV voltage, and (c) output power

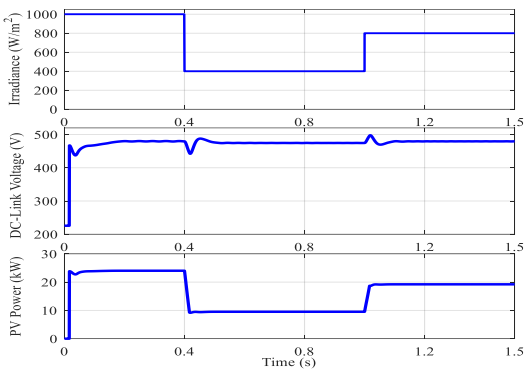

Fig. 13. The PV system's outputs for sudden step disturbances. (a) Solar radiation, (b) PV voltage, (c) output power

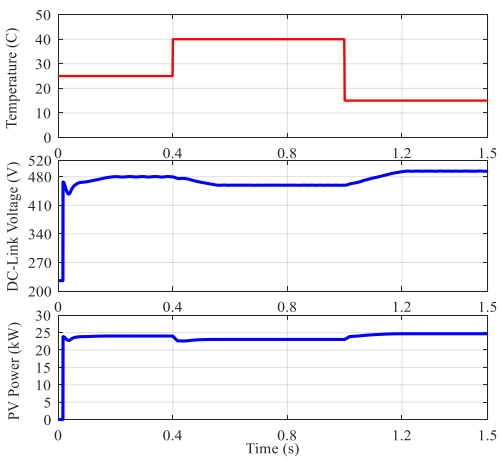

Fig. 14. The PV system's responses to step changes in temperature. (a) Temperature profile, (b) PV voltage, (c) output power

A. Converter Performance in Scenario I: PV2V Operation

To validate the stable performance of the MPPT algorithm and converter controllers ,the irradiation of 1000 W/m^2 at a fixed temperature of 25^{o}C is considered. As was already described, during the PV2V battery charging scenario, switches S_1 to S_4 on the PV side and switches S_5 and S_6 on the battery side serve as a DC chopper. Fig. 15 illustrates the results of the battery charging

during PV2V at maximum PV power of about 25 kW. Some small fluctuations are seen in voltage during the first intervals, but the converter insures 480 and 400 volts across the PV port and battery side, respectively. As illustrated in Fig. 16, the output power from PV panels (P_{PV}) is around 24 kW which is much higher than battery power (P_B), i.e., 4 kW. Therefore, in this scenario, the vehicle battery can completely charge from solar energy with no need for the power grid.

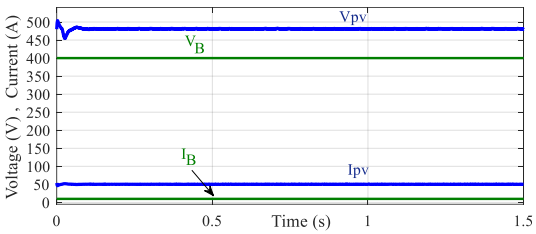

Fig. 15. The voltage and current outputs for the PV2V scenario during steady-state operation

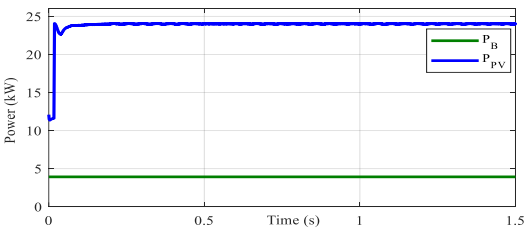

Fig. 16. The output power of the PV panels and vehicle battery for the PV2V scenario

B. Converter Performance in Scenario II: PV2G Operation

As was already explained, one of the imperative features of the proposed converter is the delivery of power to the grid when the PV output power is sufficiently high. According to Fig. 17, the current flows from the PV port to the grid and the converter acts as a grid-connected topology. Based on this scenario, the redundant power of the PV can inject into the network and feed some small loads to improve the whole system's performance.

C. Converter Performance in Scenario III: G2V Operation

Based on the aforementioned information, the battery can charge from the grid, too. Fig. 18 shows the charging operation when the battery is charged via the grid. This scenario improves the charger's reliability when the PV side suffers from environmental or seasonal conditions.

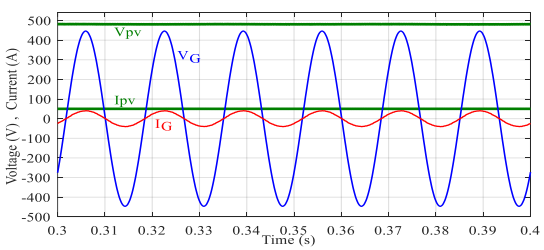

Fig. 17. The voltage and current outputs of the converter for the PV2G scenario during the steady-state operation

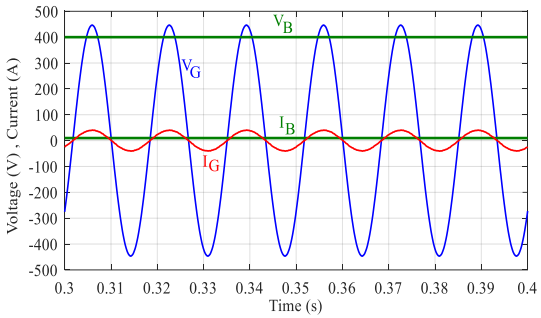

Fig. 18. The responses to the G2V scenario at the steady-state operation

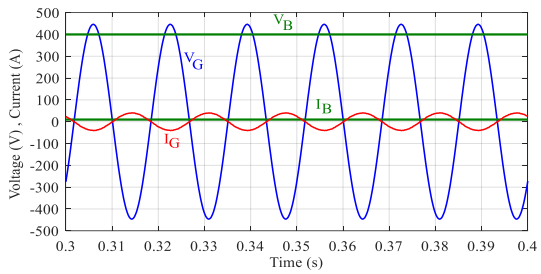

Fig. 19. The responses to the V2G scenario at steady-state

D. Converter Performance in Scenario IV: V2G Operation

Considering the proposed topology, vehicles can deliver their extra and/or unused power to the grid when needed. Hence, according to Fig. 19, battery current flows into the grid and ensures the bidirectional operation of the converter. As shown in Figs. 18 and 19, the current delivered to and from the AC grid is to be sinusoidal and in phase with the grid AC voltage which reduces current distortions and keeps a unity power factor. As illustrated in Fig. 19, the injected AC current is in the reverse direction of the grid voltage, but zero crossings points of the voltage and current still match each other.

E. Efficiency Comparison

To compare the results decently, it is better to consider the overall efficiency improvements over a wide range of parameter or variable variations. For this matter, the converter efficiency is compared for output power variations by taking the grid side voltage into account in this subsection. Fig. 20 illustrates the proposed isolated LLC converter efficiency during the scenarios in which EV batteries get charged under different voltage levels. As mentioned before, one of the key factors in battery charging is the state of charge (SOC) level which should be maintained at a rescannable rate (between 20 to 80 percent). The converter efficiency along with the output power is analyzed over the variable battery voltage from 250V to 400 V (from SOC around 60 to 100 percent, respectively) in Fig. 20. By choosing a constant input DC voltage, the efficiency declines as the output power P_O and also output current rises. On the other hand, the efficiency increases at a fixed DC-link

current. Furthermore, the maximum efficiency is around 96.3% at a power of 1 kW. Accordingly, for an appropriate SOC (around 75%), the efficiency of 96% at an output power of around 750 W for a battery voltage level of 300V is more acceptable.

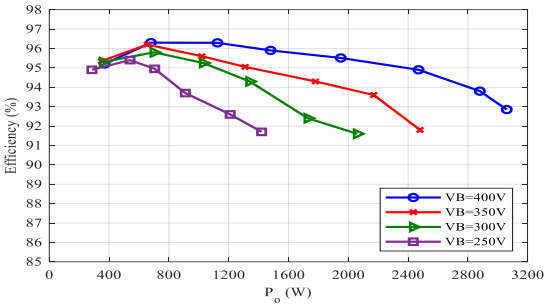

Fig. 20. The efficiency of the proposed converter during the battery charging modes

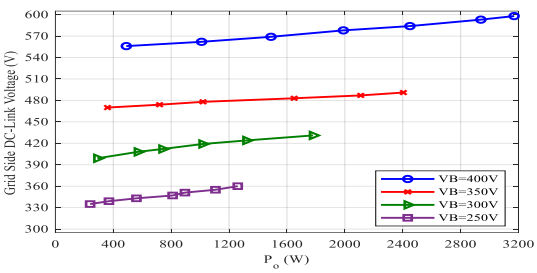

Fig. 21. The grid-side DC-link voltages during different studies using variable control of DC-link voltage.

A similar comparison study is performed in Fig. 21 which shows the grid-side DC-link voltage of the converter under different testing circumstances. Since one of the charging ports of the converter is the AC grid, the variations of DC voltage in the grid side should be analyzed to maintain not only the battery charging level but also the grid power factor. At the fixed battery voltage (V_B= 400V) and around the power related to the maximum efficiency (P_o=1 kW), the DC-link voltage is equal to 565V. For better SOC, the grid-side voltage should be maintained at 420V.

I. Conclusions

A multiport isolated DC-DC converter is studied for PEV applications by integrating the PV arrays and the power grid. The proposed converter was utilized to interface a hybrid energy system with separate sources based on different operation scenarios. As explained, the converter is designed as high power with low cost over a wide range of output voltage. A feasible unified multifunctional control system is employed to control the whole system. Considering the results, the converter operates appropriately during all different scenarios. Based on the control methodology, standard PI controllers are used to regulate the PV-side DC-link voltage, the grid-side voltage, and the battery voltage and current. The simulation results reveal that the converter is not only capable of MPPT for the PV system when solar energy is available, but can also control the charge/discharge of the vehicle battery to keep the DC-link voltage at a desired value. One of the distinguished features of the converter is the delivery of power to the battery from two ports in the lack of the PV power.

Acknowledgment

The corresponding author wishes to thank Dr. Mohsen Ebadpour for presenting and establishing the initial idea of this study named “A multiport isolated DC-DC converter for plug-in electric vehicles based on combination of photovoltaic systems and power grid” in “*12th Power Electronics, Drive Systems, and Technologies Conference (PEDSTC)*” of IEEE which was held in Tehran, Iran 2021 (see Ref. [29]). He is currently one of the manuscript authors and also the advisor in this research work.

REFERENCES

[1] Feizi M, Beiranvand R, Daneshfar M. An Integrated High Power Self-Equalized Battery Charger Using a Voltage Multiplier and Phase-Shifted Full-Bridge DC-DC Converter for Lithium-Ion Batteries. International Journal of Industrial Electronics Control and Optimization 2021; 4(2):141-155.

[2] Gonzalez A, Lopez-Erauskin R, Gyselinck J. Analysis, modeling, control and operation of an interleaved three-port boost converter for DMPPT systems including PV and storage at module level. Heliyon 2019; 5(3):1-31.

[3] Pan L, Zhang C. An Integrated Multifunctional Bidirectional AC/DC and DC/DC Converter for Electric Vehicles Applications. Energies 2016; 9(7):493.

[4] Ebadpour M, Sharifian M.B.B. Cascade H-Bridge Multilevel Inverter with Low Output Harmonics for Electric/Hybrid Electric Vehicle Applications. International Review of Electrical Engineering (IREE) 2012; 7(1): 3248-3256.

[5] Tu h, Feng H, Srdic S, Lukic S. Extreme Fast Charging of Electric Vehicles: A Technology Overview. In: IEEE Transactions on Transportation Electrification; 2019. IEEE; 2019. p. 861-878.

[6] Jyotheeswara Reddy K, Natarajan S. Energy sources and multi-input DC-DC converters used in hybrid electric vehicle applications – A review. International Journal of Hydrogen Energy 2018; 43(36):17387-17408.

[7] Yilmaz M, Krein PT. Review of battery charger topologies, charging power levels, and infrastructure for plug-in electric and hybrid vehicles. IEEE Trans Power Electron 2013; 28(5):2151-2169.

[8] Pellegrino G, Armando E, Guglielmi P. An Integral battery charger with power factor correction for electric scooter. IEEE Trans Power Electron 2010; 25(3):751-759.

[9] Zhu H, Zhang D, Zhang B, Zhou Z."A nonisolated three-port DC–DC converter and three-domain control method for PV-battery power systems. IEEE Trans Ind Electron 2015; 62(8):4937-4947.

[10] Wen G, Chen Y, Kang Y. A family of cost-efficient integrated single-switch three-port converters. In: Twenty-Eighth Annual IEEE Applied Power Electronics Conference and Exposition (APEC); 2013. IEEE; 2013. p. 1062-1067.
[11] Cheng T, Lu DDC, Gong A, Verstraete D. Analysis of a three-port DC-DC converter for PV-battery system using DISO boost and SISO buck converters. In: Australasian Universities Power Engineering Conference (AUPEC); 2015. IEEE; 2015. p. 1-6.
[12] Faraji R, Farzanehfard H. Soft-switched nonisolated high step-up three-port DC–DC converter for hybrid energy systems. IEEE Trans Power Electron 2018; 33(12):10101-10111.
[13] Kumar L, Jain S, A multiple source DC/DC converter topology. Int J Electron. Power Energy Syst 2013; 51:278-291.
[14] Li W, Xiao J, Zhao Y, He X. PWM plus phase angle shift (PPAS) control scheme for combined multiport dc/dc converters. IEEE Trans Power Electron 2012; 27(3):1479–1489.
[15] Pinto JG, Monteiro V, Goncalves H, Afonso JL. On-board reconfigurable battery charger for electric vehicles with traction-to-auxiliary mode. IEEE Trans Veh Technol 2014; 63(3):1104–1116.
[16] Wu H, Sun K, Ding S, Xing Y. Topology derivation of nonisolated three-port dc-dc converters from DIC and DOC. IEEE Trans Power Electron 2013; 28(7):3297–3307.
[17] Taheri A, Asgari N. Sliding Mode Control of LLC Resonant DC-DC Converter for Wide output voltage Range in Battery Charging Applications. International Journal of Industrial Electronics Control and Optimization 2019; 2(2):127-136.
[18] Chen Y-M, Liu Y-C, Wu F-Y. Multi-input DC/DC converter based on the multiwinding transformer for renewable energy applications. IEEE Trans Ind Appl 2002; 38(4):1096-1104.
[19] Wu H, Sun K, Chen R, Hu H, Xing Y. Full-bridge three-port converters with wide input voltage range for renewable power systems. IEEE Trans Power Electron 2012; 27(9):3965-3974.
[20] Hu W, Wu H, Xing Y, Sun K. A full-bridge three-port converter for renewable energy application. In: IEEE Applied Power Electronics Conference and Exposition – APEC; 2014. IEEE; 2014. p. 57-62.
[21] Sun X, Shen Y, Li W, Wu H. A PWM and PFM hybrid modulated three-port converter for a standalone PV/battery power system. IEEE Journal of Emerging and Selected Topics in Power Electronics 2015; 3(4): 984-1000.
[22] Zhang J, Wu H, Qin X, Xing Y. PWM plus secondary-side phase-shift controlled soft-switching full-bridge three-port converter for renewable power systems. IEEE Trans Ind Electron 2015;62(11):7061-7072.
[23] Tao H, Duarte JL, Hendrix MAM. Three-port triple-half-bridge bidirectional converter with zero-voltage switching. IEEE Trans Power Electron 2008; 23(2):782-792.
[24] Xu C et al. Performance analysis of coupled inductor based multiple-input DC/DC converter with PWM plus phase-shift (PPS) control strategy. In: IEEE ECCE Asia Downunder; 2013. IEEE; 2013. p. 994-998.
[25] Zeng J, Qiao W, Qu L.A n isolated three-port bidirectional dc-dc converter for photovoltaic systems with energy storage. IEEE Trans Ind Appl 2015; 51(4):3493–3503.
[26] Soltani Gohari H, Abbasadeh K, Gholami Gorji J. A Controllable Bidirectional Rectifier for EV Home Charging Station with G2H/G2VH/V2H/V2G Functions. International Journal of Industrial Electronics Control and Optimization 2021; 4(1):99-113.
[27] Zhao B, Song Q, Liu W, Sun Y. Overview of dual-active bridge isolated bidirectional dc-dc converter for high-frequency-link power-conversion system. IEEE Trans Power Electron 2014; 29(8):4091–4106.
[28] Jung J, Kim H, Ryu M, Baek J. Design methodology of bidirectional CLLC resonant converter for high-frequency isolation of dc distribution systems. IEEE Trans Ind Electron 2013; 28(4):1741–1755.
[29] Ebadpour M. A multiport isolated DC-DC converter for plug-in electric vehicles based on combination of photovoltaic systems and power grid. In: 12th Power Electronics, Drive Systems, and Technologies Conference (PEDSTC); 2021. IEEE; 2021. p. 1-5.
[30] Tang Y, Lu J, Wu B, Zou S, Ding W, Khaligh A. An integrated dual-output isolated converter for plug-in electric vehicles. IEEE Trans Veh Technol 2018; 67(2):966–976.
[31] Koutroulis E, Kalaitzakis K, Voulgaris NC. Development of a microcontroller-based, photovoltaic maximum power point tracking control system. IEEE Trans Power Electron 2001; 16(1):46-54.
[32] Li C, Chen Y, Zhou D, Liu J, Zeng J. A high-performance adaptive incremental conductance MPPT algorithm for photovoltaic systems. Energies 2016; 9(4):288.
[33] Mohanty S, Subudhi B, Ray PK. A grey wolf-assisted perturb & observe MPPT algorithm for a PV system. IEEE Trans Energy Convers 2017; 32(1):340-347.

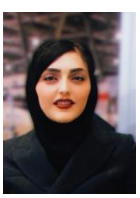

Nasim Bagheri was born in Tabriz, Iran in 1991. She received her B.Sc. degree in Biomedical Engineering from the Sahand University of Technology, Tabriz in 2013 and her M.Sc. degree in Electrical Engineering from Shabestar Azad University, Shabestar, Iran in 2015. She is a Ph.D. candidate in Electrical Engineering at Islamic Azad University, Shabestar Branch. Her current research interests include the hybrid and control of power electronic converters and their applications.

Hasan Alipour received B.Sc., M.Sc., and Ph.D. degrees in Power Electrical Engineering from the Iran University of Science and Technology (IUST), Tehran, Iran in 2008, the University of Tehran, Tehran, Iran in 2011, and the University of Tabriz, Tabriz, Iran in 2015, respectively. Currently, he is an assistant professor at the Engineering Faculty of Islamic Azad University, Shabestar Branch. His research interests include Electric and hybrid electric vehicles, electric machines drive, linear electric motors, renewable energies, and distributed generation.

Leila Mohammadian was born in Tabriz, Iran in 1984. She received her B.Sc., M.Sc., and Ph.D. degrees in Electrical Engineering from the Department of Electrical and Computer Engineering, University of Tabriz, Tabriz, Iran in 2007, 2011, and 2015, respectively. She has been with Shabestar Branch, Islamic Azad University, Shabestar, Iran since 2011. She has been an Assistant Professor since 2015. Her current research interests include the analysis and control of power electronic converters and their applications.

Jamal Beiza received his M.Sc. and Ph.D. degrees in Electrical Engineering from the Amirkabir University of Technology (AUT), Tehran, Iran in 2003 and 2009, respectively. He has been with the Department of Electrical Engineering of Islamic Azad University, Shabestar branch, Iran where he is now an Assistant Professor. His main fields of research are power system state estimation, power system operation, power system simulation, and modeling. He is a reviewer member of some scientific master Journals with the Institute for Scientific Information index. He has authored and co-authored more than 40 scientific papers.

Mohsen Ebadpour received his M.Sc. and Ph.D. degrees from the University of Tabriz, Iran, both in Electrical Power Engineering in 2011 and 2017, respectively. From March 2016 to March 2018, he had been a visiting research scholar at the Department of Electrical Engineering in the EPES research group at the University of British Columbia, Vancouver, Canada. Since 2011, he has joined the Department of Electrical Engineering, Islamic Azad University where he became an Assistant Professor in 2017. Currently, he is serving as an Associate Research Fellow in Research and Innovation Center for Electrical Engineering (RICE) with the University of West Bohemia in Pilsen, Czech Republic. He is the author and co-author of more than 30 journal and conference papers. His research interests include electrical machine drive control, modeling and analysis of power electronic converters, and fault-tolerant control.